CHAPTER II
LITERATURE REVIEW

In order to achieve the metal oxide thin film multilayer with desired properties for this work, a basic understanding of sputtering technology, metal oxide thin films, and thin films for optical applications are required. Additional background information is provided relating to the structural and optical characterizations of thin films. This information gives an overview of the fundamental knowledge for this study.

2.1 Metal Oxide Thin Films

Metal oxides play a significant role in many areas of physics, chemistry and materials science. The metal elements are able to form a large diversity of oxide compounds. Metal oxides have been wildly used in optical applications because of its tunable properties, excellent optical transparency, and chemical and environmental stability (Park *et al.,* 2017). Common metal oxide coating materials are SiO_2, TiO_2, Al_2O_3, Nb_2O_5, HfO_2 and Ta_2O_5. Silicon dioxide (SiO_2) and titanium dioxide (TiO_2) are the famous coating materials due to their excellent properties and mass production ability.

2.1.1 Silicon Dioxide Thin Film

Silicon dioxide, also known as silica and its chemical formula is SiO_2, is a main compound extensively found in quartz and sand. Its atomic weight is 60.08 g/mol. Silicon dioxide is an oxide formed by Si^{+4} and O^{-2}. The compound is mostly found in the crystalline form by a cation Si central, coordinated to 4 anion O, so that the structure of silica has a tetrahedral geometry. It also exists in amorphous solid or other crystalline forms as rhombohedral, hexagonal, cubic, nonclinical or ortorhombic geometry. The chemical structure model of silicon dioxide can be shown as the below figure. It is a transparent to gray, odorless, crystalline or amorphous solid, and insoluble in water and acid. Its melting and boiling point are 1600 °C and 2230 °C, respectively.

It has energy bandgap of 8.9 eV approximately. Its density is 2.65 g m/L. For the chemical properties, silicon dioxide is not very reactive compound since the polarity of molecule is zero. The Si forms two double bonds with the oxygen, so it is extremely stable.

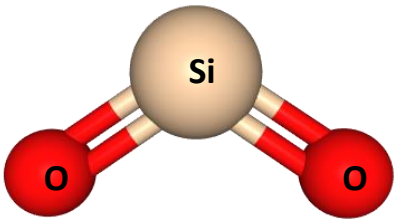

Figure 2.1 Chemical Structure Model of silicon dioxide. (Adapted from https://pubchem.ncbi.nlm.nih.gov/compound/24261).

For using as coating material, silicon dioxide has an inexpensive price, low refractive index, high transmittance from the ultraviolet (UV) to near infrared (NIR) region, good insulation and chemical and mechanical properties. Coupling of silicon dioxide layer with a high refractive index material can be done for making optical multilayer films (Wang *et al.,* 2018). In addition, SiO_2 films are a important part in semiconductor industry due to their high resistivity, good dielectric strength, large band gap, high melting point, and native, low defect density interface with Si (Šimurka *et al.,* 2018). SiO_2 band gap with the value of 8.9±0.1 eV were shown in Seguini 's paper. There are several methods to produce silicon dioxide thin films, for example, DC and RF magnetron sputtering (Lee *et al.,* 2006 and Jeong *et al.,* 2004), ion beam sputtering (Wang *et al.,* 2018), electrospinning (Raut *et al.,* 2013), sol–gel (Dou *et al.,* 2016), dip-coating (Chi *et al.,* 2011).

Šimurka studied the optical and mechanical properties of amorphous SiO_2 thin films deposited on soda-lime silicate float glass by reactive RF magnetron sputtering at room temperature. The sputtering chamber was evacuated to a base pressure lower than 1.2×10^{-4} Pa before starting the deposition.

Moreover, in order to clean the surface of the silicon target before each deposition, 5 min of pre-sputtering was performed. The magnetron power remained

the same at 300 W during reactive sputtering. The deposition parameters of each sample are shown in Table 2.1. The dependence of the process pressure on the properties was examined. The film densities are strongly influenced by the process pressure and shift between 2.38 and 1.91 g/cm^3 as the pressure changes from 0.27 to 1.33 Pa.

Table 2.1 Deposition parameters (Šimurka *et al.,* 2018).

Sample	Pressure		Argon	Oxygen	Deposition rate
	(mTorr)	(Pa)	(sccm[a])	(sccm[a])	(nm.min^{-1})
S2	2	0.23	18.7	2.4	8.3
S4	4	0.53	18.7	2.3	11.3
S6	6	0.80	18.7	2.3	12.4
S10	10	1.33	18.7	2.3	10.1

[a]Standard cubic centimeters per minute

Figure 2.2 shows the evolution of surface morphology with increasing process pressure. As can be seen, the arithmetic and root mean square roughness (Ra and rms) increase significantly with increasing process pressure. On the other hand, density exhibits opposite trend and decreases with the pressure from 2.38 to 1.91 g cm^{-3} (Table 2.2).

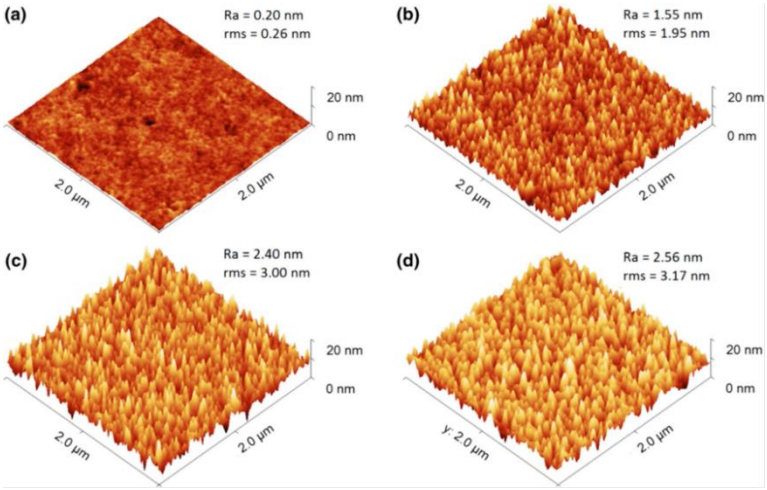

Figure 2.2 Surface morphology of the films deposited at different process pressures (a) 0.27 Pa, (b) 0.53 Pa, (c) 0.80 Pa, (d) 1.33 Pa (Šimurka *et al.,* 2018).

Table 2.2 Roughness values (Ra and rms) of the SiO_x films obtained by AFM, their thickness and density obtained by XRR) (Šimurka *et al.,* 2018).

Sample	Pressure(Pa)	Ra(nm)	rms (nm)	Thickness(nm)	Density(g.cm^{-3})
S2	0.27	0.20	0.26	269	2.38 ± 0.01
S4	0.53	1.55	1.95	327	2.16 ± 0.01
S6	0.80	2.40	3.00	298	1.98 ± 0.05
S10	1.33	2.56	3.17	192	1.91 ± 0.01

Figure 2.3 shows the Si 2p XPS spectra measured at the film surface referenced to C 1s at 284.8 eV. The result revealed a stable position of Si 2p (~ 103.2 eV) typical for stoichiometric O/Si = 2.0 ratio for films prepared at the pressure ranging from 0.53 to 1.33 Pa. For the sample S2 deposited at the lowest pressure of 0.27 Pa, the Si 2p peak shifts to lower binding energy (103.0 eV) with substoichiometric O/Si = 1.8 ratio. Shift to the lower binding energies indicates the presence of suboxide structure suggesting

that the oxygen flow was not sufficient to fully oxidize the sputtered silicon resulting in $SiO_{1.8}$ thin film.

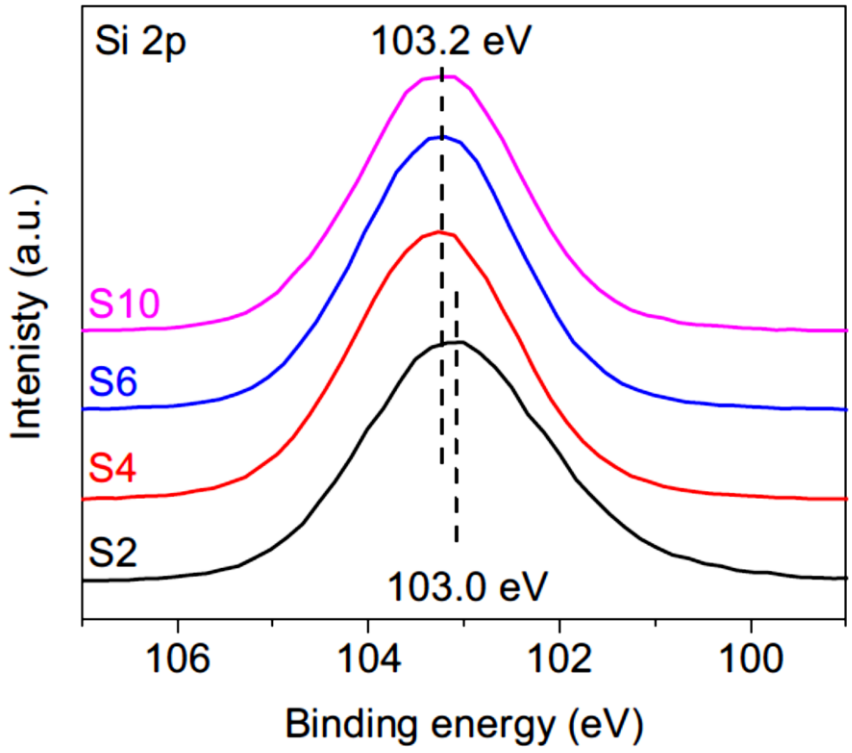

Figure 2.3 High-resolution Si 2p XPS spectra measured at the film surface referenced to C 1s at 284.8 eV (Šimurka *et al.,* 2018).

For the optical properties Figure 2.4 shows the refractive index of the prepared films. As can be seen, the refractive index decreases with the increasing process pressure in the whole spectral range. Figure 4b illustrates the development of refractive index with the film density at the wavelength of 632.8 nm. The refractive indices of the films vary between 1.37 and 1.52 when density increases from 1.91 to 2.38 g/cm^3. All the films exhibit high transparency and do not significantly vary from the transparency of the glass substrate (Figure 4). Only approximately 1.3% lower transmittance in the visible light region was observed for the sample S2 deposited at the lowest process pressure (Figure 2.5). This decrease in transmittance can be attributed to the suboxide structure detected by XPS.

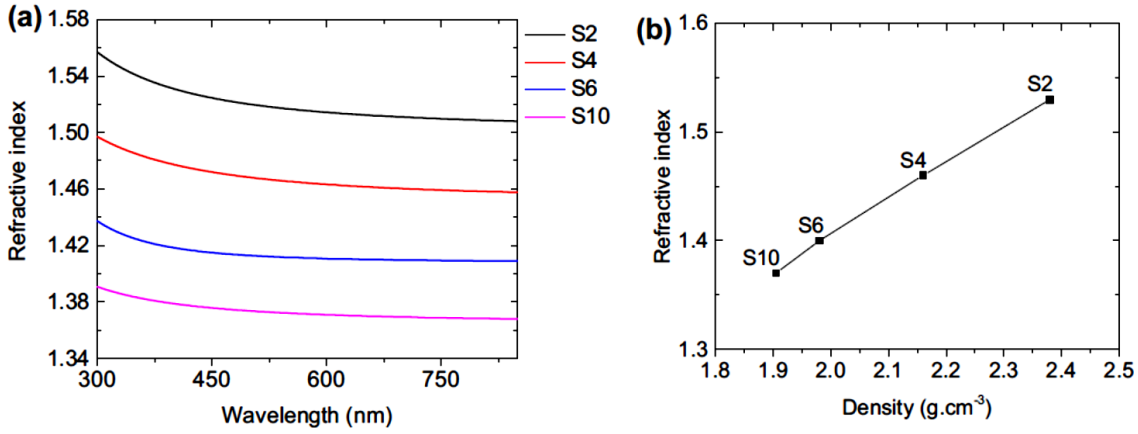

Figure 2.4 Refractive index of the films a as a function of the optical wavelength for samples S2, S4, S6 and S10, and b at 632.8 nm as a function of film density (Šimurka *et al.,* 2018).

Fujiyama *et al.* studied the effect of O_2 partial pressure on the mechanical properties of SiO_2 films deposited by rf magnetron sputtering using SiO_2 target with a purity of 99.99%. Figure 2.6 indicates the deposition rate of SiO_2 films as a function of the O_2 partial pressure, where the flow rate of argon gas is 10 cm^3/min. The deposition rate clearly decreases by 35% due to the addition of the O_2 gas into the argon atmosphere. In addition, the rate is independent on the existence of O_2 partial pressure. The composition of sputtered SiO_2 films in pure argon gas is deficient in oxygen compared to that for bulk SiO_2, but it is close to that of bulk SiO_2 when oxygen gas with a pressure of above about 2×10^{-2} Pa is added.

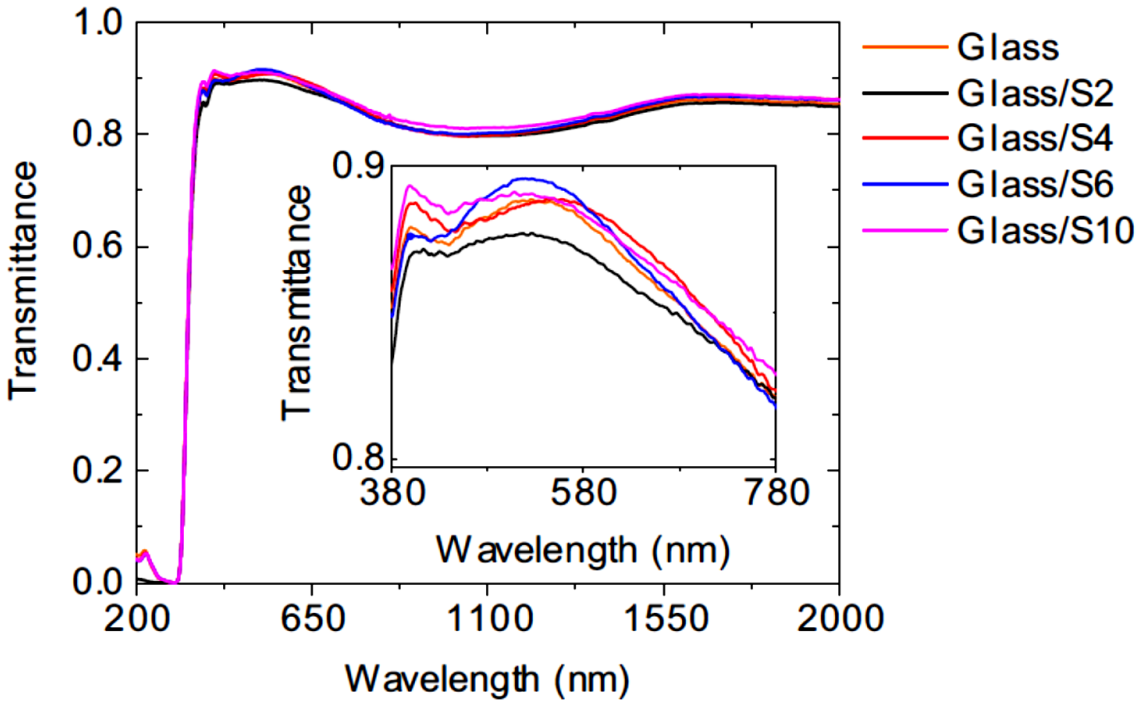

Figure 2.5 Optical transmittance of the glass substrate and systems glass/film (Šimurka *et al*., 2018).

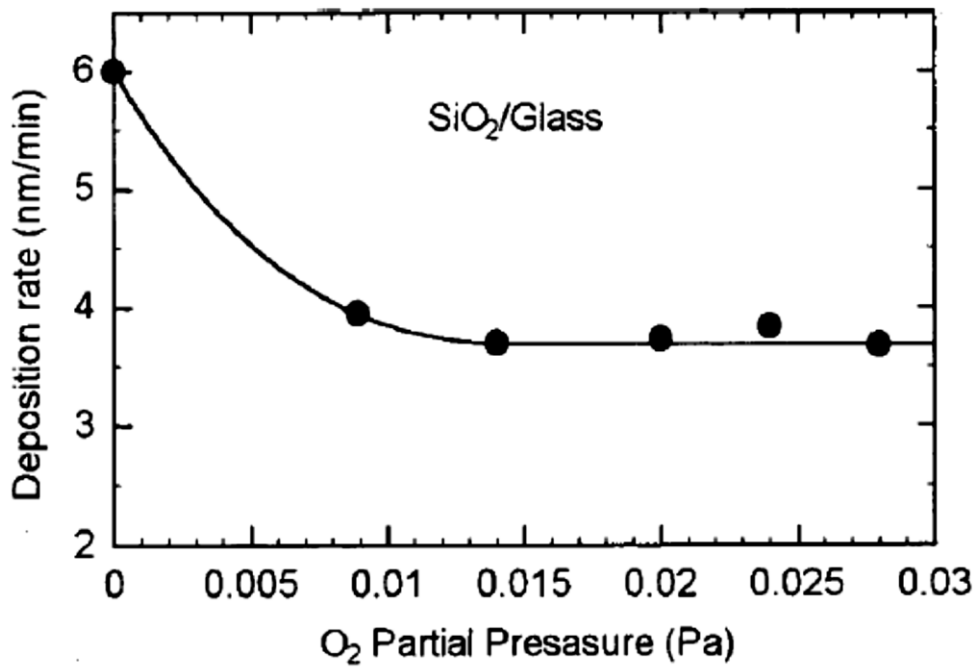

Figure 2.6 Sputtering rate with added oxygen to that without oxygen for 1 mm film thickness deposited at 8×10^{-2} Pa as a function of oxygen partial pressure (Fujiyama *et al*., 2002).

Table 1. The density, thickness and root-mean-square surface roughness of the deposited SiO_2 layer for samples A1, A2, A3 and A4 ascertained from XRR

Sample	Density (g cm^{-3})	Thickness (nm)	Roughness (nm)
A1	2.35	75.32	1.16
A2	2.34	75.82	0.84
A3	2.35	81.39	0.80
A4	2.33	79.90	0.67

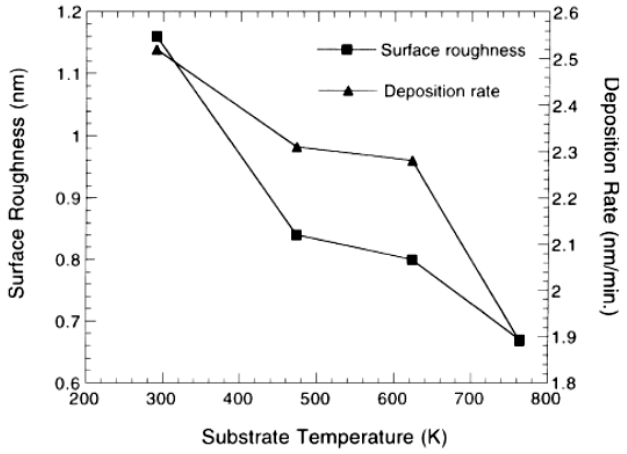

Table 2. The density, thickness and root-mean-square surface roughness of the deposited SiO_2 layer for samples B1, B2, B3 and B4 ascertained from XRR

Sample	Density (g cm^{-3})	Thickness (nm)	Roughness (nm)
B1	2.28	49.77	0.51
B2	2.32	67.22	0.70
B3	2.26	70.18	1.51
B4	2.37	70.83	2.38

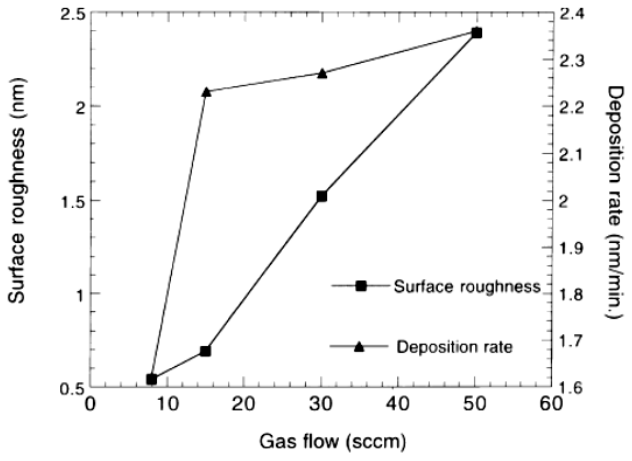

Figure 2.7 The surface roughness (nm) and deposition rate (nm /min) (Left) vs. substrate temperature (K) (Right) vs. argon gas flow (sccm) (Kojima *et al*., 1999).

Kojima *et al*. studied grazing-incidence XRR characterization of as-grown SiO_2 thin films deposited on Si(100) substrates by rf magnetron sputtering with various substrate temperatures and gas flow rates. The results show that an increase of substrate temperature from room temperature to 763 K only slightly decreases the surface roughness (Figure 2.7). Comparatively, the surface morphology is strongly controlled by the gas flow conditions during deposition. The surface roughness increases almost linearly from 0.51 to 2.38 nm when the argon flow rate is increased from 8 to 50 sccm (Figure 7). The XPS results confirm that it is possible to prepare high-quality SiO_2 thin films by the sputtering method.

2.1.2 Titanium Dioxide Thin Film

Titanium dioxide (TiO_2) usually occurs in amorphous form and also in three crystalline polymorphs: anatase, rutile and brookite. The most abundant and most extensively studied polymorph is the rutile phase. Anatase and rutile phases are tetragonal in nature while brookite exhibits an orthorhombic structure (Figure 2.8) (Esch *et al*., 2014).

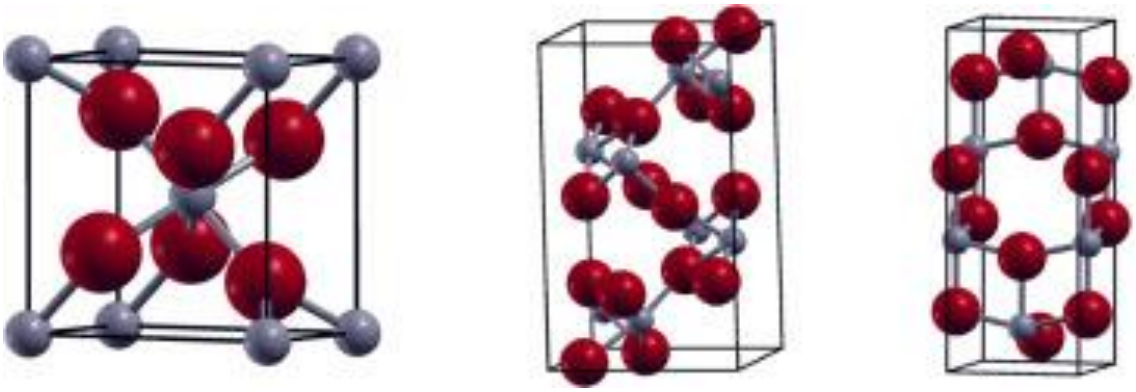

Figure 2.8 The primitive cells of rutile, brookite and anatase (from left to right, Esch *et al*., 2014).

TiO_2 has melting and boiling points of 1840 °C and 2900 °C, respectively. For physical properties, titanium dioxide is an odorless and tasteless white crystalline powder. The bulk density of rutile phase is 4.13 g/cm^3. It has a band gap of 3.0 eV (Zhang *et al*., 2014). The rutile structure is very compact and thermodynamically most stable phase at all temperatures, and has higher refractive index than anatase (2.7 vs 2.52, at 550 nm wavelength). Rutile phase exhibits better optical activity than anatase

and is used for antireflective and dielectric applications (Nair *et al*., 2014). Moreover, the rutile is widely used as a white pigment material due to good scattering effect that protects material from ultraviolet radiations (Nair *et al*., 2011).

Titanium dioxide thin films are used in a wide range of applications, such as gas sensors, photocatalysis, solar cells, optical devices, etc. They have high optical transmittance with high refractive index in the visible range, outstanding chemical stability, high photocatalytic activity, good mechanical hardness and non-toxicity (Pjević *et al*., 2015). Different techniques can be used to fabricate TiO_2 films, for example, DC and RF magnetron sputtering, chemical vapor deposition (CVD), Pulsed laser deposition (PLD), hydrothermal method and Sol-Gel (Wang *et al*., 2017).

Kang *et al.* study the effect of crystallization in TiO_2 thin films on optical properties characterized by transmittance measurements using UV-VIS spectrophotometry. TiO_2 thin films with amorphous and anatase phases were prepared using an RF sputtering and a TiO_2 (99.99%) target with a 5-cm diameter. Deposition process was performed at an RF power of 120 W. The TiO_2 films were deposited on quartz substrates at room temperature for 120 min. The distance between the target and substrate was 10 cm and the sputtering gas was Ar (20 sccm). The base pressure of the chamber was less than 6.67×10^{-3} Pa, and the working pressure was approximately 1.33×10^{-1} Pa.

Amorphous and anatase TiO_2 films were obtained by post-annealing in a tubular furnace at temperatures of 550 °C for 120 min in air. Figure 2.9(a) – (c) show the surface morphologies of the TiO_2 films with post-annealing. The grain growth indicating crystallization occurred when the film was postannealed at 550 °C, and the morphology with dense surface and no grain was obtained in the film post-annealed at 900 °C. Figure 2.9(d) shows the XRD pattern of the as-grown TiO_2 film and TiO_2 films post-annealed at 550 and 900 °C.

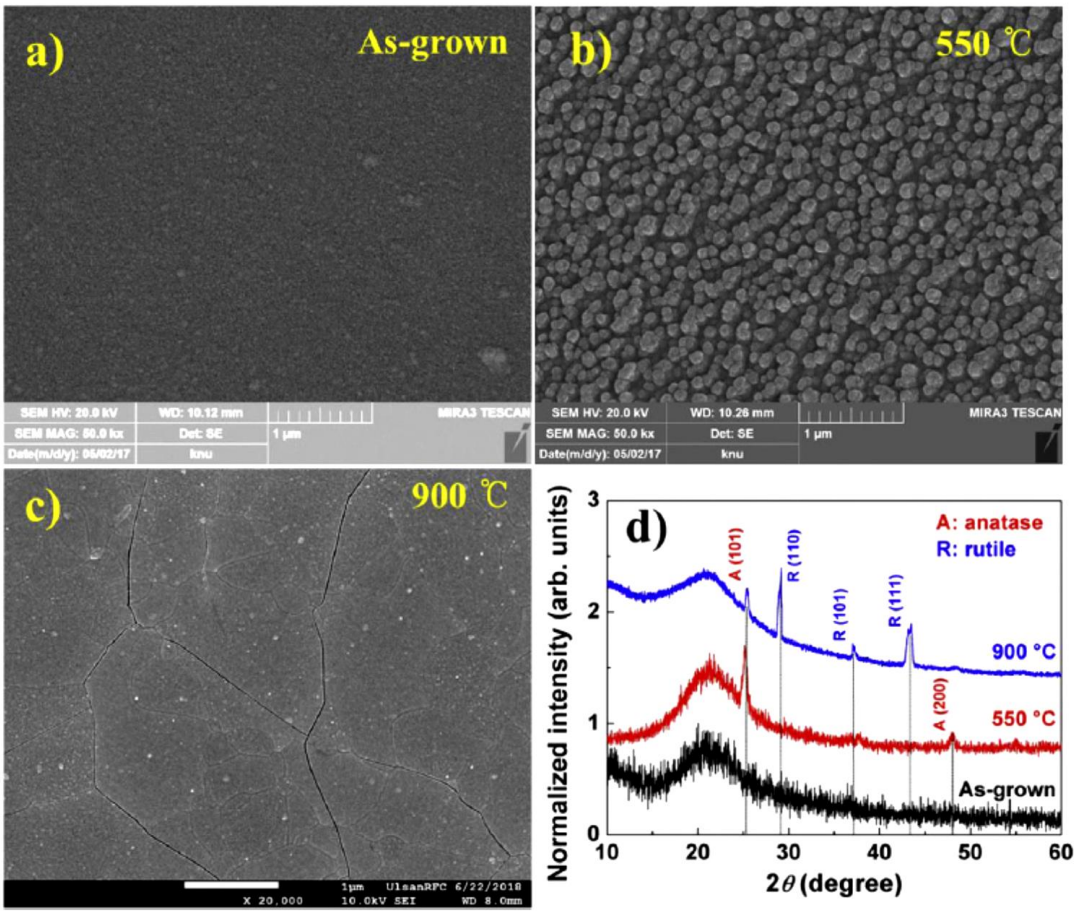

Figure 2.9 Surface morphologies of the TiO_2 films with different post-annealing temperature: (a) as-grown film, (b) film post-annealed at 550 °C, and (c) at 900 °C. (d) XRD patterns of the as-grown film and films post-annealed at 550 °C and 900 °C (Kang *et al*., 2018).

The optical transmission spectra of the TiO_2 polymorph films were shown in Figure 2.10. The films have a high transmittance of ~80%, and the fundamental absorption edge at a wavelength of approximately 360 nm. The absorption edge shifts slightly toward longer wavelengths with increasing post-annealing temperature (Figure 10 inset). This results from the crystallization because of the post-annealing. Additionally, the optical constant spectra of the films showed a gradual change above 3.5 eV.

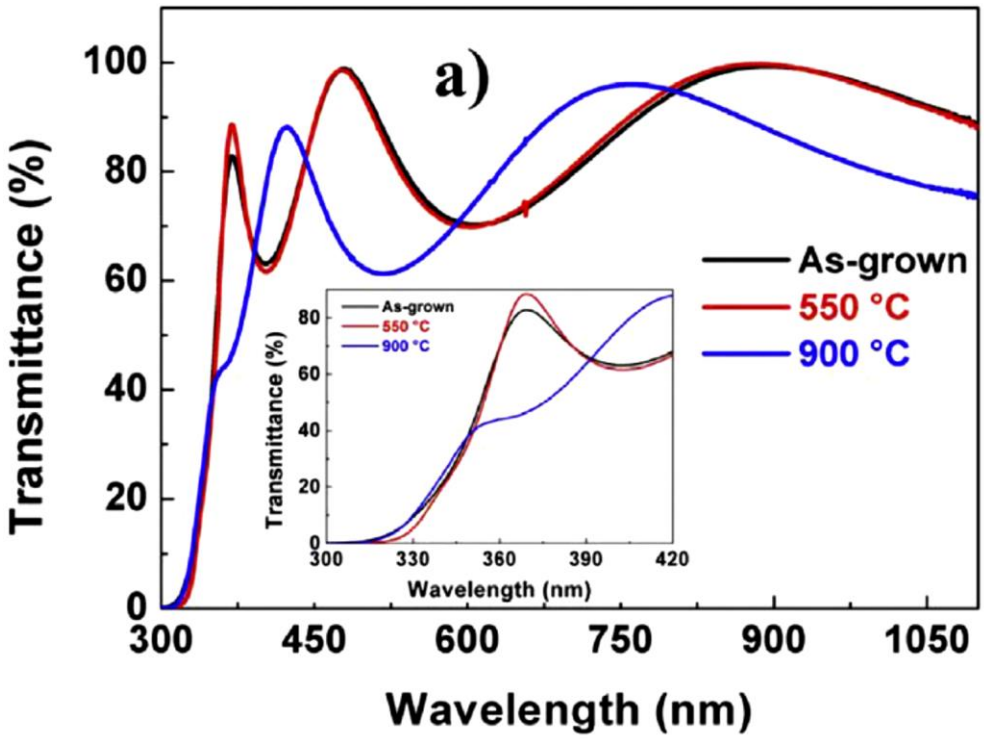

Figure 2.10 Optical transmission spectra of TiO_2 polymorph films (Kang *et al*., 2018).

Nair *et al.* studied the optical parameters induced by phase transformation in RF magnetron sputtered TiO_2 thin films which were deposited onto quartz substrates using a ceramic TiO_2 target at a pressure of 0.01 mbar, a power of 300W and a substrate temperature of 573 K. Thermal annealing to the prepared film for 2 h at 873 K in air produced the formation of anatase phase, and a phase transformation to rutile with rod-like surface morphology was observed at 1073 K. The refractive index increased with increase in annealing temperature (Figure 2.11) because rutile is the optically active phase.

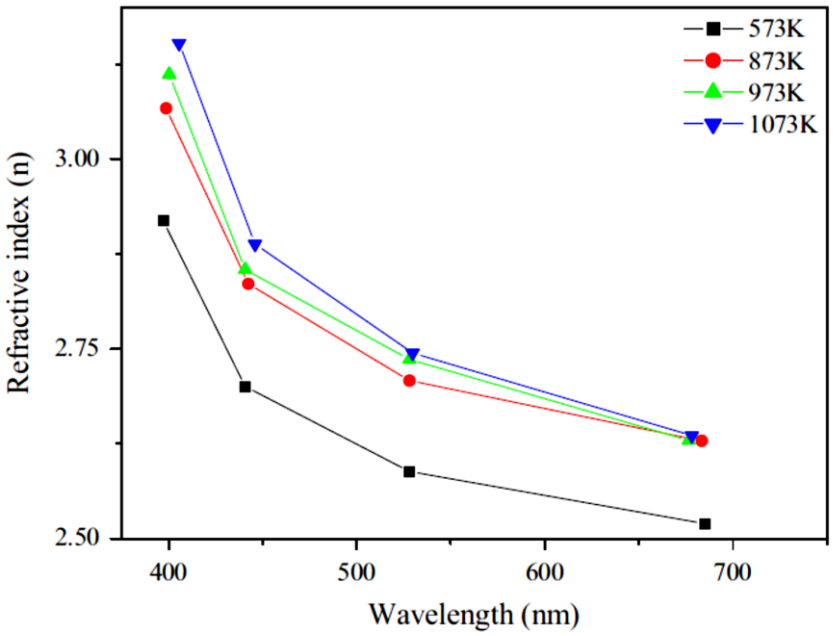

Figure 2.11 Plot of refractive index versus wavelength for as-deposited and annealed TiO_2 thin films (Nair *et al.,* 2014).

Grayeli Korpi *et al*. reported influence of the oxygen partial pressure on the growth and optical properties of RF-sputtered anatase TiO_2 thin films. Titanium dioxide films with thicknesses around 300 nm were deposited on glass substrates by reactive RF magnetron sputtering using a pure TiO_2 target at constant RF sputtering power (200 W), high working pressure (5×10^{-3} Torr) and room temperature. The details of samples are given in Table 2.3 which indicate that the surface roughness and crystallinity are noticeably dependent on the presence of small oxygen concentrations during the preparation. The grain size of the films and the surface roughness significantly decrease when the O_2 addition is increased. Figure 2.12 shows the XRD patterns of TiO_2 films deposited at different $O_2/(Ar + O_2)$ ratios. These diffraction patterns show three well-defined peaks corresponding to the planes (1 0 1), (2 0 0) and (2 1 1) of the anatase crystalline phase (JCPDS 21-1272). The intensity of the anatase peaks depends on the oxygen concentration in the chamber during sample preparation, increasing the peak intensities as the $O_2/(Ar + O_2)$ ratio from 0 to 0.2, and decreasing again for $O_2/(Ar + O_2)$ = 0.3. It was noticed that an excessive presence of oxygen during film deposition obstructs the crystallization of the anatase phase.

Table 2.3 Grain size (D), average surface roughness (R_{ave}) and thickness calculated with the Sanepoel method of samples produced at various O_2/Ar + O_2 ratios (Grayeli Korpi *et al*., 2017).

Samples	O_2/Ar + O_2 ratio	D (nm)	R_{ave} (nm)	thickness (nm)
1	0	144.2	18.9	304.12
2	0.1	121.5	14.2	299.51
3	0.2	26.0	3.4	295.94
4	0.3	18.1	2.0	295.06

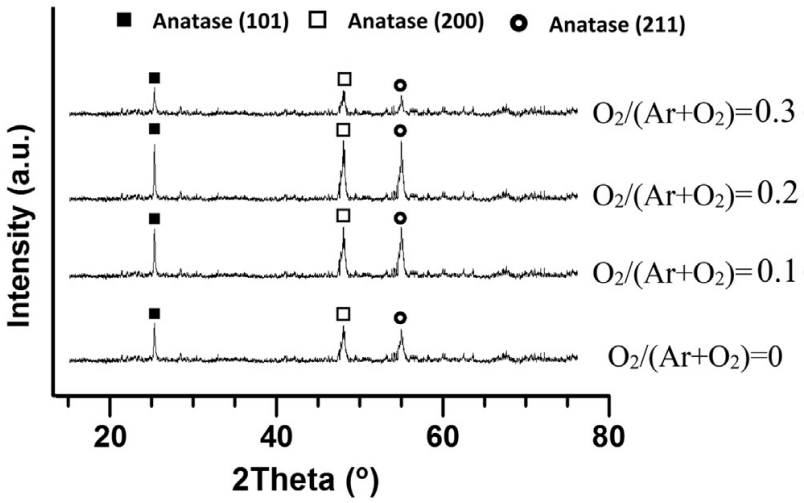

Figure 2.12 XRD patterns of various samples produced at different O_2/Ar + O_2 ratios (Grayeli Korpi *et al*., 2017).

For optical results, the transmittance spectra of the TiO_2 films at various O_2/Ar + O_2 ratios are shown in Figure 2.13. The average transmittance of the different samples is approximately 85% in the visible region respecting to reference blank glass substrate. When the sample prepared under pure Ar ambient, the transmittance in visible light is decrease, probably due to its larger surface roughness.

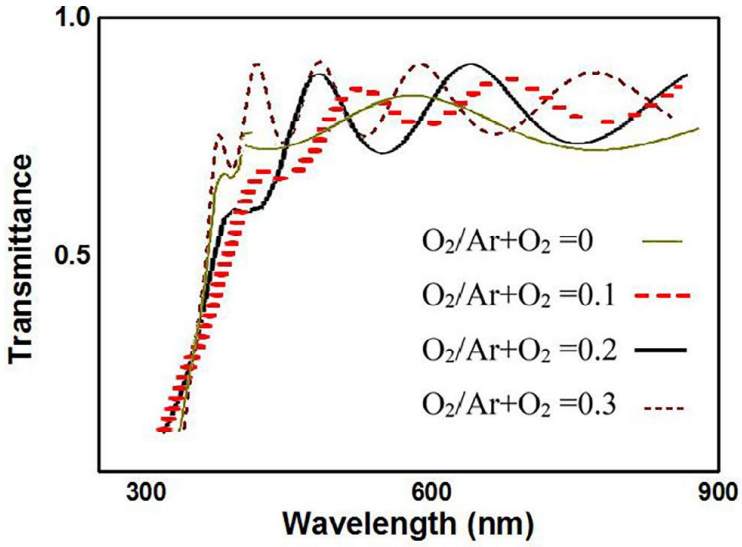

Figure 2.13 Optical transmittance spectra of various samples produced at different O_2/ Ar + O_2 ratios (Grayeli Korpi *et al*., 2017).

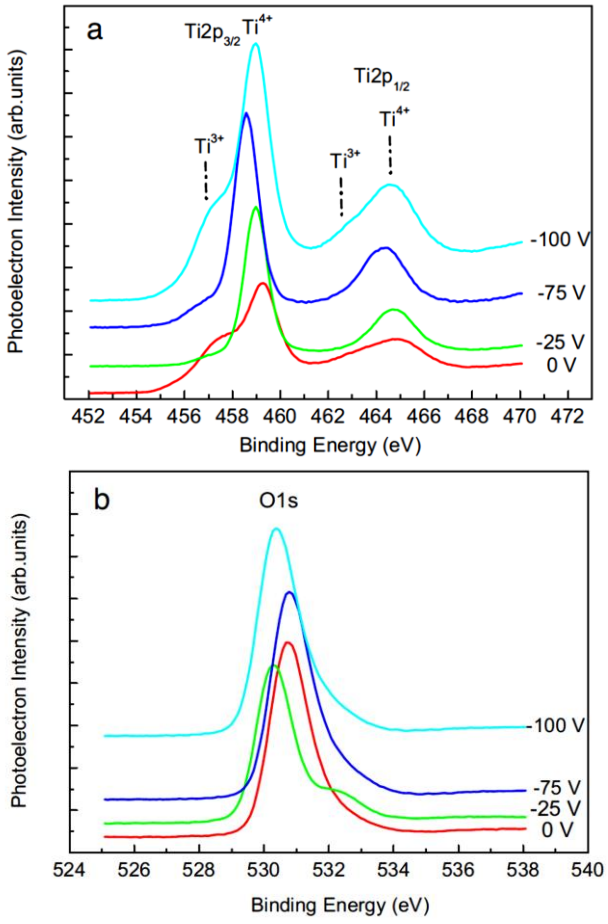

Figure 2.14 Ti2p (a) and O1s (b) XPS spectra of TiO_2 thin films (Nezar *et al.*, 2017).

Nezar *et al*. show that it is possible to deposit nanocrystalline anatase TiO_2 thin films on both biased and unbiased glass substrates by controlling the sputtering conditions. Pure metal titanium target (99.99%) was used as a sputtering target. The sputtering gas and reactive gas were pure argon (99.99990%) and pure oxygen (99.99%) respectively. The voltage applied to the substrate was varied (0, −25, −50, −75 and −100 V) whereas all other deposition parameters were constant (sputtering power = 250 W, deposition time = 60 min, working gas pressure = 2.66 Pa, 25% of oxygen flow rate, and room temperature). XPS results revealed that titanium atoms were present on the form of Ti^{4+} state corresponding to the chemical composition of TiO_2 (Figure 2.14).

2.1.3 Other Metal Oxide Thin Film

Besides SiO_2 and TiO_2, other metal oxide such as Al_2O_3, HfO_2 and Ta_2O_5 are common metal oxide coating materials for optical applications. HfO_2 and Ta_2O_5 films are one of the most important high refractive index materials from the ultraviolet to near-infrared region. Ta_2O_5 films are the preferred high-refractive-index materials in the field of ultra-low loss laser films, and HfO_2 films are the preferred high refractive index materials in the field of high laser damage threshold films (Wang *et al.,* 2017). Wang *et al.* studied the effects of hot-isostatic pressing and annealing post-treatment on HfO_2 and Ta_2O_5 films prepared by ion beam sputtering. In the aspect of optical properties, both post-treatment methods can increase physical thickness and reduce refractive index and extinction coefficient. Figure 2.15 shows effect of hot-isostatic pressing and annealing treatment on optical constants of HfO_2 and Ta_2O_5 films

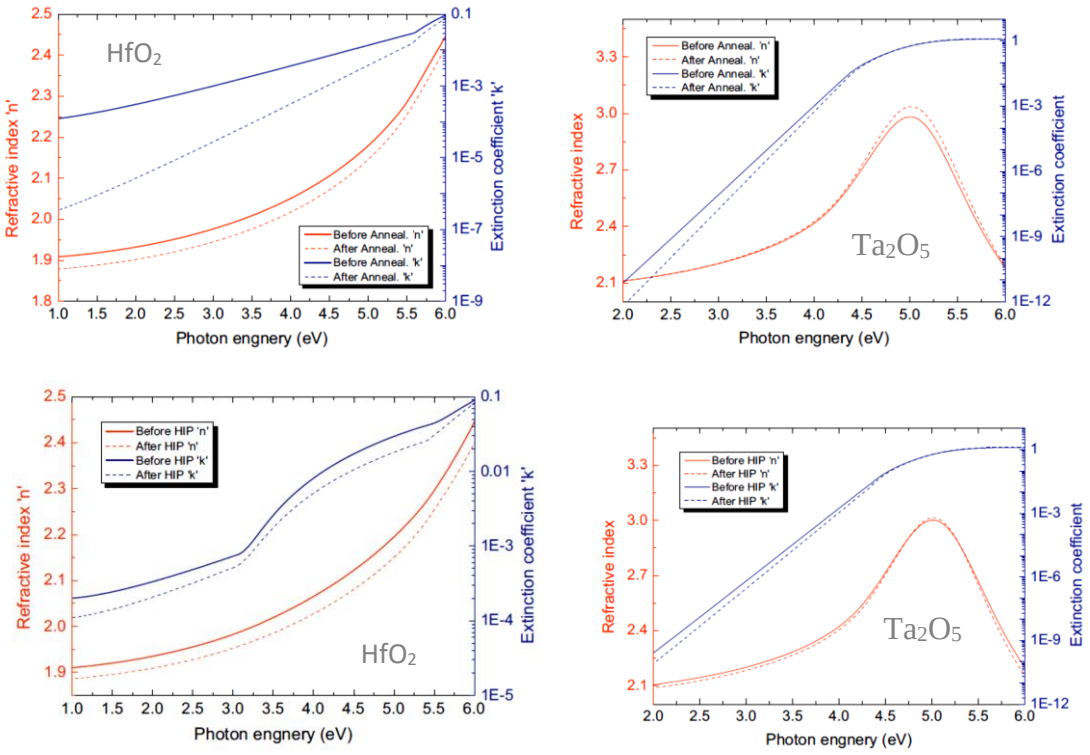

Figure 2.15 Effect of hot-isostatic pressing and annealing treatment on optical constants of HfO_2 and Ta_2O_5 films (Wang *et al.,* 2017).

Kesmez *et al*. fabricated single layer and multilayer films consisting of SnO_2, Ta_2O_5, SiO_2, TiO_2, indium tin oxide (ITO) and antimony tin oxide (ATO) by sol-gel dip coating technique. Table 2.4 indicates the light transmittance, thickness, refractive index and roughness of single layer films and light transmittance of multilayer films. Among the single layer films, porous SiO_2 film had the highest light transmittance of 95%. Figure 2.16 present the light transmittance plots of single layer films as a function of wavelength. It is obvious that the highest transmittance can be achieved in the SiO_2 film in the 300–900 nm region. All of the studied oxides except silicon dioxide resulted in a decrease in the light transmittance comparing with uncoated glass when applied in single layer form. This was expected, since the refractive indices of these oxides are higher than that of the glass.

Table 2.4 Light transmittance(Measured by Hazameter, at 550 nm), refractive indices and thickness values of single layer films and light transmittance values of multilayer films (Kesmez *et al*., 2018).

Sample	%Light Transmittance	Reflective index	Film thickness (nm)	Roughness (rms)(nm)
Bare glass	89.5	-	-	-
SiO_2	95	1.36	103	1.20
Ta_2O_3	86.7	1.70	34	8.95
ATO	87.1	1.64	38	11.46
ITO	89	1.54	30	7.83
SnO_2	86.9	1.67	71	2.30
TiO_2	89.1	1.99	115	23.44
ITO-TiO_2-SiO_2	97.5	-	-	-
ITO-Ta_2O_5-SiO_2	96.2	-	-	-
SnO_2-TiO_2-SiO_2	94.9	-	-	-
SnO_2-Ta_2O_5-SiO_2	95.1	-	-	-
ATO-TiO_2-SiO_2	80.4	-	-	-

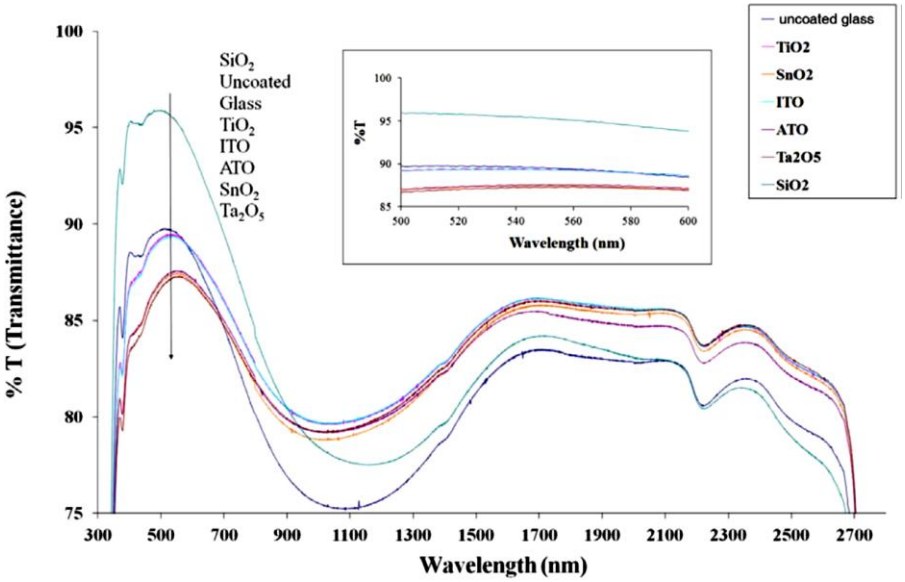

Figure 2.16 % light transmittance spectra of single layer films (Kesmez *et al*., 2018).

2.2 Thin Films for Optical Applications

2.2.1 Interference in thin films

Basically, interference effects are commonly observed in thin films, such as thin layers of oil on water or the thin surface of a soap bubble. The varied colors observed when white light is incident on such films result from the interference of waves reflected from the two surfaces of the film. Consider a film of uniform thickness *t* and refraction index (RI) *n*. The wavelength of light λ_n in the film is

$$\lambda_n = \frac{\lambda}{n} \quad (1)$$

where λ is the wavelength of the light in free space and *n* is the refractive index of the film material. Let's assume light rays traveling in air are nearly normal to the two surfaces of the film as shown in Figure 2.17. Reflected ray 1, which is reflected from the upper surface (A) in Figure 17, undergoes a phase change of 180° with respect to the incident wave. Reflected ray 2, which is reflected from the lower film surface (B), undergoes 180° phase change because it is reflected from a glass that has a higher reflective index than that of film. Therefore, ray 1 is in phase with ray 2. We must also consider, however, that ray 2 travels an extra distance $2dcos\theta_2$ before the waves recombine in the air above surface A. If $2dcos\theta_2 = \lambda_n$, rays 1 and 2 recombine in

phase and the result is constructive interference. In general, the condition for constructive interference in thin films is (Serway *et al*., 2014)

$$2dcos\theta_2 \ = m\lambda_n \ \ m = \ 0, 1, 2, \ldots \tag{2}$$

Because $\lambda_n = \ \lambda/n$, Equation 2 can be written as

$$2ndcos\theta_2 \ = m\lambda \quad , m = \ 0, 1, 2, \ldots \tag{3}$$

If the extra distance $2dcos\theta_2$ traveled by ray 2 corresponds to a multiple of λ_n, the two waves combine out of phase and the result is destructive interference. The general equation for destructive interference in thin films is

$$2ndcos\theta_2 \ = \left(m + \frac{1}{2}\right)\lambda \quad , m = \ 0, 1, 2, \ldots \tag{4}$$

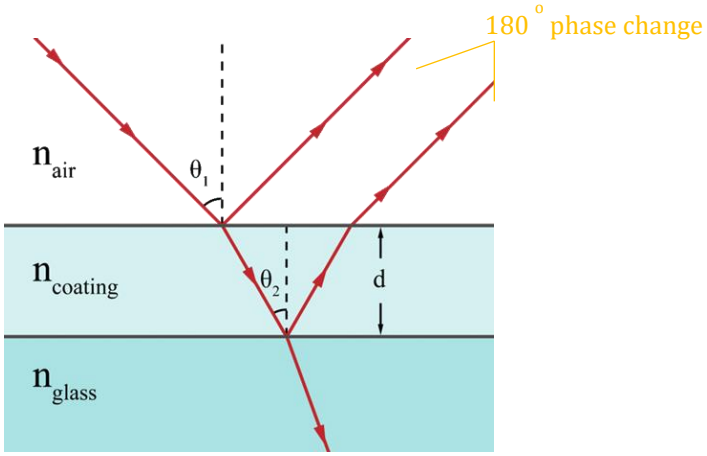

Figure 2.17 Light paths through a thin film on glass (https://en.wikipedia.org/wiki/Thin-film_inter-ference).

2.2.2 Multilayer thin films

A multilayer coating consisting of *m* thin homogeneous and isotropic layers on a thick substrate is considered as shown in Figure 2.18. Normally, a film is considered to be thin in the case when full interference effects are observable in the reflected or transmitted light. At a boundary between two media, denoted by suffix 0 for the incident medium and by suffix 1 for the exit medium, the incident beam is split into a

reflected beam and a transmitted beam. For normal incidence, we have the amplitude reflection *r* and transmission *t* coefficients are: (Macleod, H.A., 2010).

$$r = \frac{\eta_o - \eta_1}{\eta_o + \eta_1} \tag{5}$$

$$t = \frac{2\eta_o}{\eta_o + \eta_1}, \tag{6}$$

where η is optical admittance.

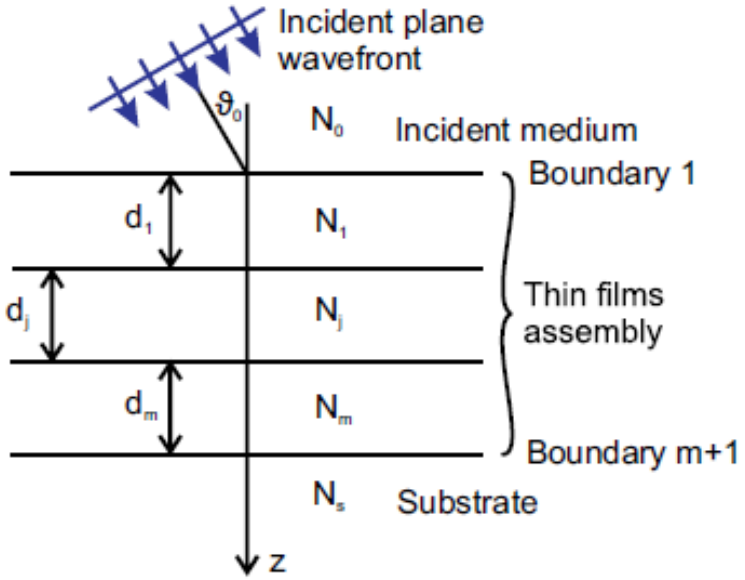

Figure 2.18 Schematic of a multilayer thin films (Fedulova et al., 2016).

In order to avoid fundamental difficulties, the incident medium is considered to be absorption-free, which means η_o is real, then the intensity transmission and reflection coefficients (transmittance *T* and reflectance *R*) are given by:

$$R = \left(\frac{\eta_o - \eta_1}{\eta_o + \eta_1}\right)\left(\frac{\eta_o - \eta_1}{\eta_o + \eta_1}\right)^* \tag{7}$$

$$T = \frac{4\eta_o \mathrm{Re}(\eta_1)}{(\eta_o + \eta_1)(\eta_o + \eta_1)^*} \tag{8}$$

The reflectance of an assembly of thin films is calculated through the concept of optical admittance. We replace the multilayer by a single surface (Macleod, H.A., 2010), which presents an admittance *Y* that is the ratio of the total tangential magnetic and electric fields and is given by

$$Y = C/B \tag{9}$$

Where $$\begin{bmatrix} B \\ C \end{bmatrix} = \left\{ \prod_{r=1}^{q} \begin{bmatrix} cos\delta_r & (isin\delta_r)/\eta_r \\ i\eta_r\, sin\delta_r & cos\delta_r \end{bmatrix} \right\} \begin{bmatrix} 1 \\ \eta_m \end{bmatrix} \tag{10}$$

$\delta_r = 2\pi Nd\ cos\vartheta/\lambda$ (ϑ is the angle between the ray and normal line to film boundary) and η_m = substrate admittance.

The order of multiplication is important. If q is the layer next to the substrate, then the order is

$$\begin{bmatrix} B \\ C \end{bmatrix} = [M_1][M_2]\cdots[M_q] \begin{bmatrix} 1 \\ \eta_m \end{bmatrix} \tag{11}$$

M_1 indicates the matrix associated with layer 1, and so on. Y and $\boldsymbol{\eta}$ are in the same units. As in the case of a single surface, $\boldsymbol{\eta}_o$ must be real for reflectance and transmittance to have a valid meaning. By using the general characteristic matrix of an assembly of m thin layers, then the basic formulas for calculating spectral characteristics of a multilayer coating are given as follows:

$$R = \left(\frac{\eta_o B - C}{\eta_o B + C}\right)\left(\frac{\eta_o B - C}{\eta_o B + C}\right)^* \tag{12}$$

$$T = \frac{4\eta_o \mathrm{Re}(\eta_s)}{(\eta_o B + C)(\eta_o B + C)^*} \tag{13}$$

In order to design multilayer thin film for optical application, free or commercial software can calculate the performance of an assembly and help as a guideline before fabrication.

In 2012, Han, K. *et al*. fabricated TiO_2/SiO_2 multilayer film structure by the sol–gel synthesis with thermal treatment processes. Removing the hydrophobic alkoxy groups from the pre-deposited film surface is necessary to fabricate well defined multilayer film structures, as shown in Figure 2.19b. Figure 2.20 shows FE-SEM images of the 2nd TiO_2 film surfaces including the contact angle photographs on the 1st SiO_2 films for the 250nm TiO_2 film. The 1st SiO_2 surface characteristics were varied with sintering conditions which affect the amounts of the residual ethoxy groups ($Si(OC_2H_5)_4$ used as a SiO_2 precursor) on the surface (proved by FTIR spectra). The higher amounts

of the residual ethoxy groups on the surface, the lower the surface energy to overcome the surface tension of the coating solution (Figure 2.19a). The well-defined TiO_2/SiO_2 multilayer essembly was successfully fabricated at a sintering temperature of 300 °C by forming a hydrophilic SiO_2 layer with the heating-up period (Han, K. *et al*., 2012).

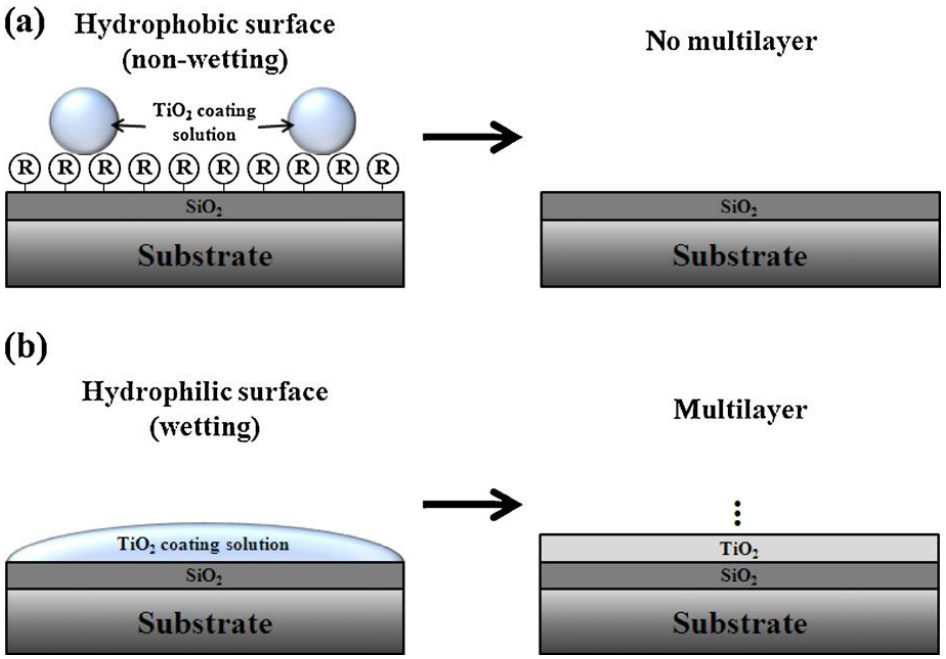

Figure 2.19 Schematics of (a) hydrophobic and (b) hydrophilic surfaces of the SiO_2 film. The R represents alkoxy group remained after sintering on the SiO_2 film surface. TiO_2 coating solution was applied to the SiO_2 film surfaces to fabricate the multilayer structure (Han, K. *et al*., 2012).

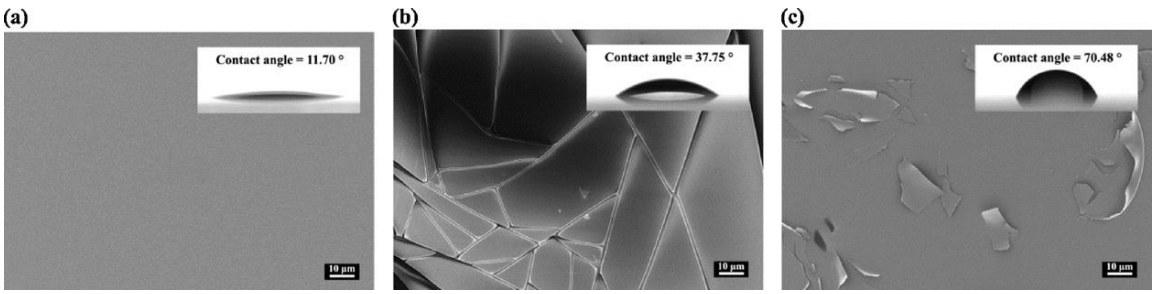

Figure 2.20 Examples of FE-SEM images of the 2nd TiO_2 250nm film surfaces for (a) clear, (b) cracks, and (c) delamination morphologies. The inserted contact angles were measured on the 1st SiO_2 films before deposition of the 2nd TiO_2 film (Han, K. *et al*., 2012).

2.2.3 Anti - Reflective Coating

The optical phenomenon, reflection is born out of a transition in the medium in which light is travelling. The mathematical model or the vector method to deduce the condition for anti-reflection considers a single layer thin film (refractive index, RI = *n*) on a glass substrate (RI = n_s) as shown in Figure 2.19. The interference effect is considered under the two following assumptions: (1) the reflected waves have the same intensity and one reflected wave per interface and (2) other optical interactions such as scattering, absorption etc. are negligible. Therefore, from Figure 2.21, if ray 1 and ray 2, the two reflected waves, undergo a destructive interference, thereby cancelling each other, there would be no reflection. From this follow the two essential criteria for Anti-Reflection. The reflected waves are π radians out of phase or the phase difference, δ is $n\pi/2$. The thickness of the film (*d*) is an odd multiple of $\lambda/4$ where λ is the wavelength of the incident beam. As the equation governing phase difference is $\delta = 2\pi nd\ cos\theta/\lambda$, substituting the value of δ and d, we get $\theta = 0$, that is normal incidence. The reflectance at normal incidence is given by (Raut *et al*., 2011)

$$r = \left[\frac{n_{air}n_s - n^2}{n_{air}n_s + n^2}\right]^2 \quad (14)$$

Where, n_s, n_{air} and n are refractive index of the substrate, air and film respectively

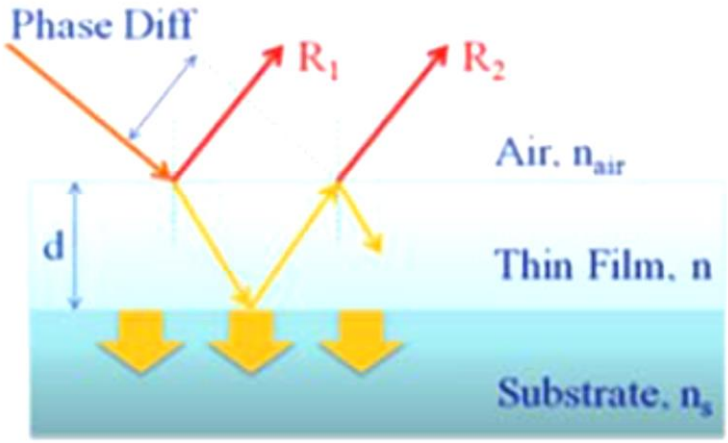

Figure 2.21 Propagation of light rays through a single layer film on substrate ($n_s > n$) (Raut *et al*., 2011).

As the objective is to achieve zero reflectance, R is set to zero and the refractive index of the film (*n*) is found to be $\sqrt{n_{air}n_s}$. The fact that reflectance (*R*) proposed by Fresnel is dependent on the s and p-polarization of the light, the anti-reflective property is also analyzed on the basis of those parameters (Raut *et al*., 2011).

2.2.4 High Reflection Coating

For the metal multi-dielectric mirror coatings, the basic principle, illustrated in Figure 2.22, consists in enhancing the reflectivity of a metal film at a given wavelength band by exploiting interference effects in thin films. A high reflectivity (*R*) metal layer (Al: *R* ~ 92%; Ag: *R* ~ 96%) is overcoated with one or several pairs of transparent films of high (H) and low (L) refractive index. For this purpose, dielectric films like SiO_2, MgF_2 (L-materials) or HfO_2, Nb_2O_5, TiO_2 (H-materials) are used. For the selection of the coating materials, properties like residual stress, adherence, resistivity to abrasion and humidity, and coating yield are of importance. The optical thickness of the layers is usually chosen to be $\lambda/4$. The dielectric coatings lead, therefore, to a wavelength-and angle dependent modulation of the reflectivity. The larger the ratio of the refractive index of the LH pair, the higher is the peak reflectivity and width of the enhanced region. Adding LH pairs, optimized for the same wavelength, will increase the reflectivity but narrow down the useful range. The layer stack terminates usually with a H-layer (Braem *et al*., 2005).

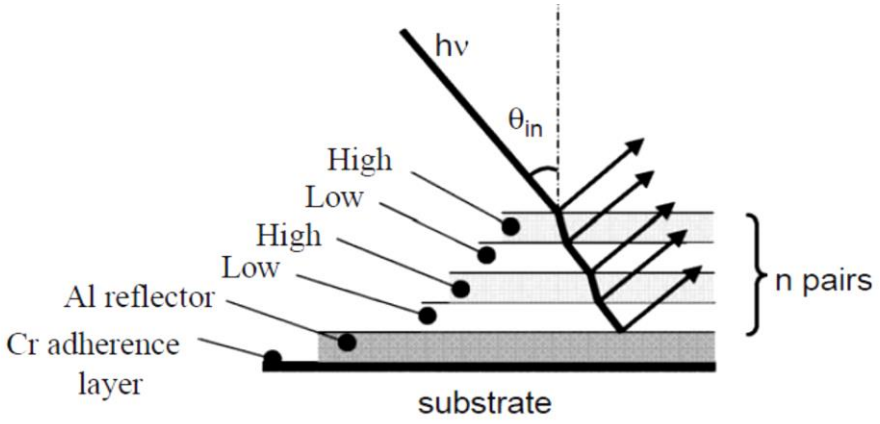

Figure 2.22 Schematic representation of a metal multi-dielectric mirror (Braem *et al*., 2005).

Dubey, R. S. *et al*. fabricated of TiO_2/SiO_2 stacks based Bragg reflectors by using sol-gel spin coating technique. The prepared single-layer thin films of TiO_2 and SiO_2 onto glass substrates were characterized for their optical constants. One-seven distributed Bragg reflectors (DBR) stacks of TiO_2/SiO_2 were prepared by tuning the process parameters. The refractive indices (by using Filmetrics, F20) of TiO_2 and SiO_2 films are 2.2 and 1.4 respectively. By increasing of the number of DBR stacks, the reflectance increased with the shift towards higher wavelength range as shown in Figure 2.23.

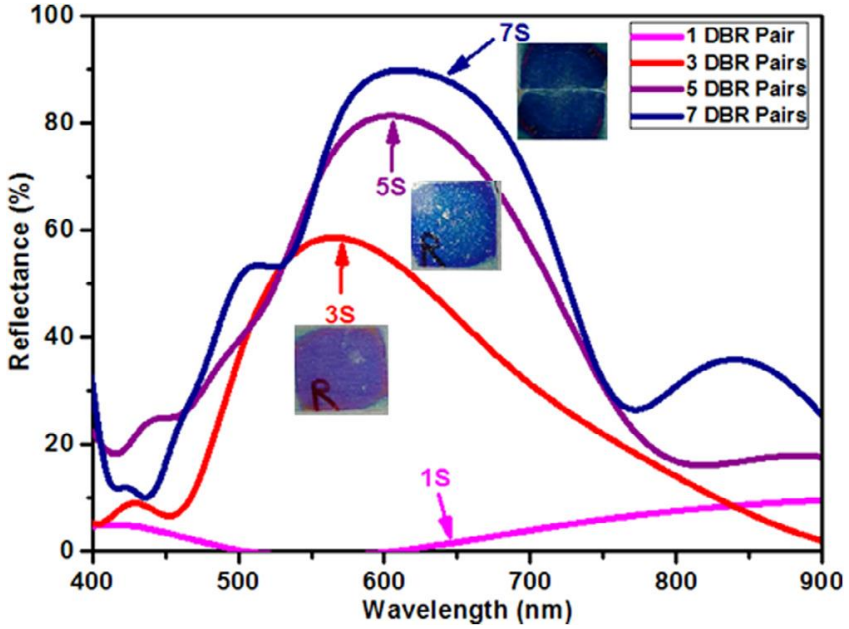

Figure 2.23 Reflectance spectra of one-, three-, five- and seven-DBR stacks with their optical images (Dubey, R. S. *et al*., 2017).

In Han, K. *et al*.'s study in 2011, multilayer structure consisting of H/L/H ($TiO_2/SiO_2/TiO_2$) refractive index materials were prepared by sol–gel method and spin coating process (Figure 22). Film thicknesses were examined by spectroscopic ellipsometry (SE) and focused ion beam (FIB) techniques (Figure 2.24), and refractive indices of TiO_2 and SiO_2 single layer films were also measured by SE. Figure 2.25 shows the n and k values of TiO_2 and SiO_2 single layer films (Han, K. *et al*., 2011).

Theoretical calculations and experimental data for the UV–Vis–NIR reflectance spectra from the multilayer film are shown in Figure 24. Experimental reflectance is in

good agreement with the theoretical prediction using constant refractive index for the NIR region, but it shows moderate deviation at the wavelength lower than 700 nm. It is possibly due to the large variation of the refractive index of TiO_2, as shown in Figure 23. The highest reflectance on the NIR region was obtained with the quarter-wave condition at λ=1000 nm (Han, K. *et al*., 2011).

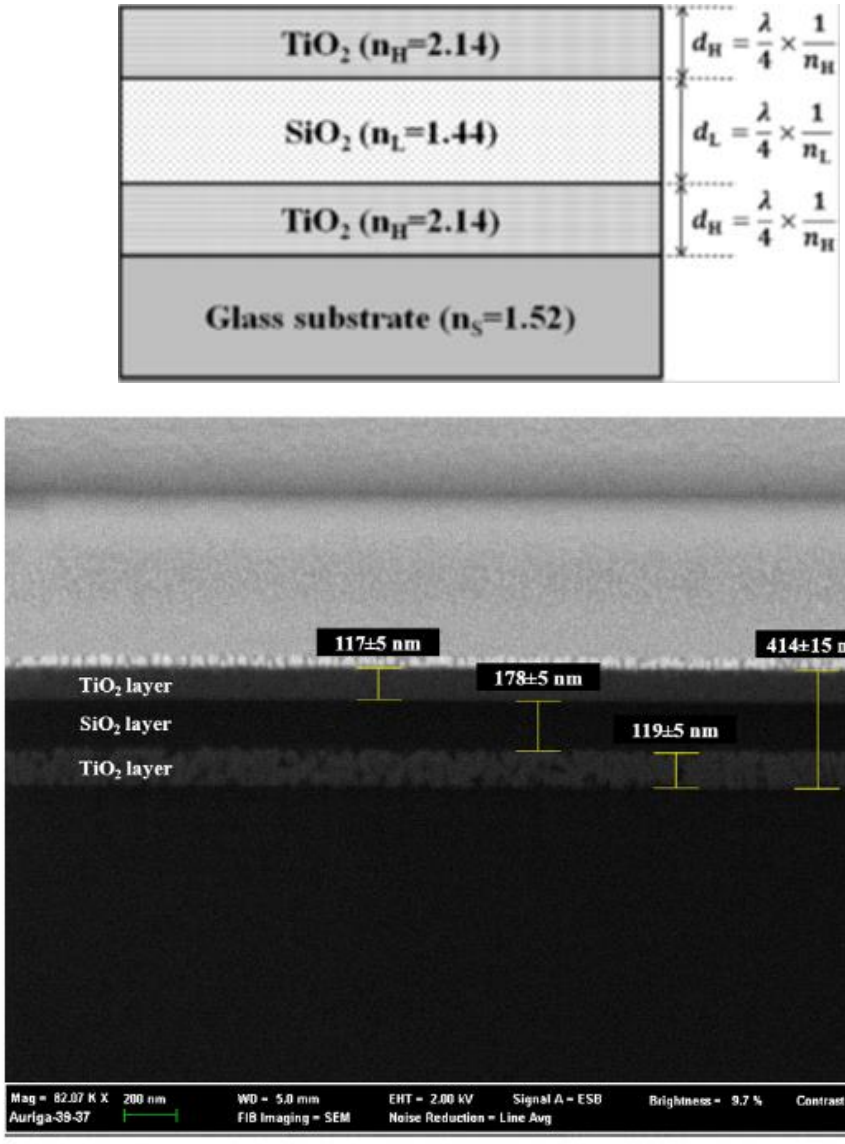

Figure 2.24 (Left) Schematic of a multilayer structure (Right) A FIB image (SEM) of a multilayer structure (Han, K. *et al*., 2011).

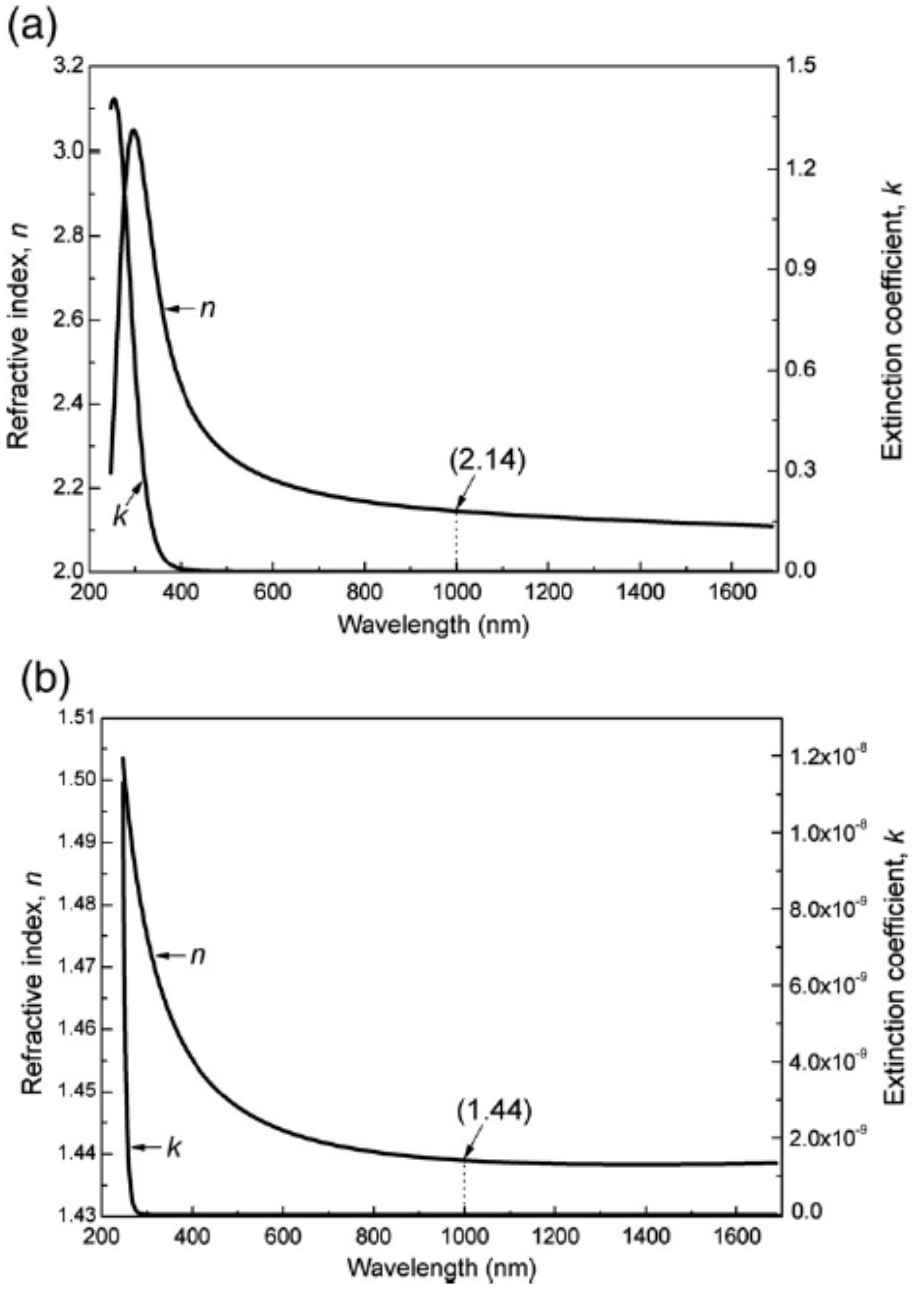

Figure 2.25 Optical constants (*n* and *k*) measured for (a) TiO_2 and (b) SiO_2 films (Han, K. *et al*., 2011).

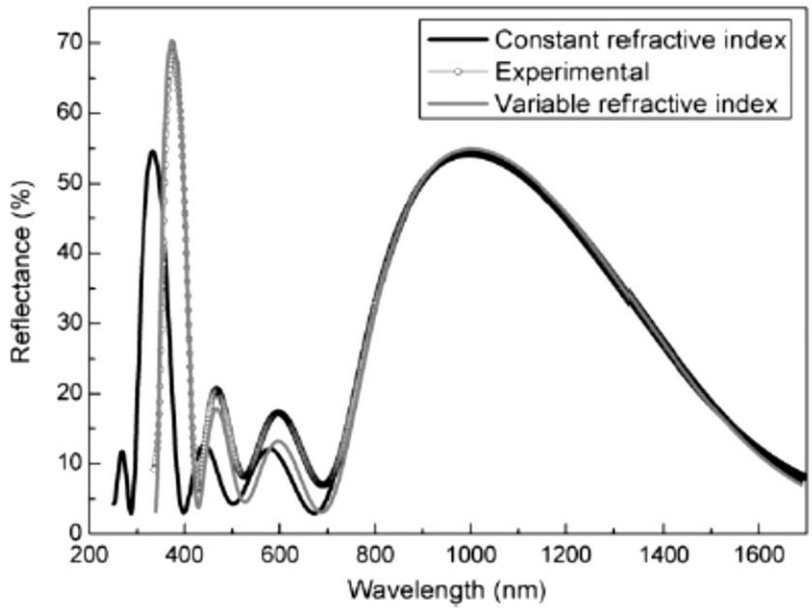

Figure 2.26 UV–Vis–NIR reflectance spectra from calculations and experimental measurement at the quarter wave condition (Han, K. *et al.,* 2011).